Broadband shock vibration absorber based on vibro-impacts and acoustic black hole effect

Haiqin Li, Patrick O'donoughue, Florent Masson, Adrien Pelat, François Gautier, Cyril Touzé

Broadband shock vibration absorber based on vibro-impacts and acoustic black hole effect

Haiqin Li[a,b,c,*], Patrick O'Donoughue[b], Florent Masson[d], Adrien Pelat[b], François Gautier[b], Cyril Touzé[c]

[a] *Tianjin Key Laboratory of Nonlinear Dynamics and Control, Department of Mechanics, Tianjin University, Tianjin 300350, China*
[b] *Laboratoire d'Acoustique de l'Université du Mans, UMR CNRS 6613, Avenue Olivier Messiaen, 72085 Le Mans, Cedex 09, France*
[c] *IMSIA, ENSTA Paris-CNRS-EDF-CEA, Institut Polytechnique de Paris, 828 Boulevard des Maréchaux, 91762 Palaiseau Cedex, France*
[d] *MVB Engineering, ACOEM Group, 200 Chemin des Ormeaux, 69760 Limonest, France*

Abstract

A vibration absorber combining the acoustical black hole (ABH) effect with vibro-impacts is presented as a separate device that can be mounted on a primary structure for passive vibration mitigation. The vibration isolator is shown to be effective for low-frequency shock vibration attenuation. Numerical and experimental results are reported, considering a rectangular honeycomb plate as the primary structure, on which the device, consisting of a circular ABH plate with one or several impact masses, is attached. A numerical model is developed using a finite element space discretisation combined with a conservative scheme in a penalty approach for the contact dynamics. The analysis shows that the device has broadband efficiency thanks to the combined effects of energy transfer due to impacts and high attenuation in mid and high-frequency range due to the ABH effect. A detailed parametric study underlines that the tuning of the linear fundamental frequency of the impact mass plays an important role. Besides, considering several impact masses is shown to improve the efficacy. An experimental setup is then used in order to demonstrate the effectiveness of the device. The results confirm the vibration mitigation trends obtained from the numerical model that could then be used as a designed tool for the attenuator. Finally, an analysis based on the Shock Response Spectrum (SRS), widely used in the field of aerospace engineering, is performed, underlining the attenuator is able to reduce rapidly and efficiently the vibrations due to a mechanical shock.

Keywords: Vibration absorber; Acoustic Black Hole; Vibro-impact; Shock isolation; Energy transfer; Honeycomb plate.

*Corresponding author.
Email address: lihaiqin1992@tju.edu.cn (Haiqin Li)

1. Introduction

The effective control of unwanted vibration in a passive manner using vibration absorbers that can act with broadband efficacy, has been a subject of special concern in many fields of engineering. Since the pioneering work of den Hartog and the advent of the tuned vibration absorber [1], enlarging the efficacy of an absorber in order to extend its frequency range has been of concern, and numerous different strategies have been proposed, using for example an essential nonlinearity in order to create a nonlinear energy sink (NES) [2–4], impact dampers [5] or friction dampers [6], nonlinear tuned vibration absorber [7, 8], negative linear stiffness [9] or combinations of multiple effects including magnetic forces or piezoelectric shunts [10–15].

Concomitantly, a growing interest emerged in passive techniques using a tapered profile of the host structure in order to create the so-called Acoustic Black Hole effect (ABH). From the pioneering works [16, 17], a large body of literature has been devoted to unfolding the principle of the method, based on the decrease of the wave velocity in the tapered area, leading to an important localization of vibration energy. Combined with increased absorption in the same region provided *e.g.* by an added viscoelastic layer, ABH can be viewed as an anechoic structural termination localized at the boundary. Numerous characterization of the phenomenon have been reported both theoretically and experimentally, underlining the impressive efficacy of the vibration mitigation in the mid- and high-frequency range, see *e.g.* [18–21] for characterization of damping properties, [22–24] for numerical optimizations of the effect, [25, 26]for analytical illustrations, [27–30] for experimental demonstrations, and [31, 32] for recent surveys. With regard to ABH effects, recent developments consider for example wave manipulations and investigation of band gaps [33–35], energy harvesting [36–38], innovative geometrical designs including folds or rings [39–43], inclusions in metamaterials [44, 45], added effects due to negative stiffness [46], and creation of the effect by an added electrical circuit creating a virtual acoustic black hole [47].

A known limitation of the acoustic black hole effect is linked to the existence of a *cut-on* frequency, below which the efficiency severely decreases. The cut-on frequency has been defined using various approaches, based on geometrical considerations [48, 49], following a phase point of view [50] from the analysis of dispersion relations [25], or in terms of localization [51]. In order to bypass this limitation, the intentional use of nonlinearity has been proposed in order to achieve energy transfer and consequently improve the low-frequency efficacy. The geometric nonlinearity, that is in any case excited given the terminal thickness of ABH design, has been specifically used in [52]. The use of contact nonlinearity has then been numerically investigated in [53, 54], in order to create a so-called Vibro-Impact ABH (VI-ABH). Experimental demonstrations have been highlighted in [55]. Other designs involving additional linear and/or nonlinear vibration absorbers have also been numerically studied in [56], whereas an electrical circuit is appended to the ABH in [57] to create the nonlinearity.

In most of the studies, the tapered region that defines the ABH is embedded inside the primary structure and viewed either as an anechoic termination or an interior zone where the vibrational energy is localized and damped out. This configuration provides a suitable

coupling between the black hole region acting as an absorber and the region outside it. More recently in the ABH litterature, it has been proposed to use the ABH effect in an external device that can be appended to the primary structure as a vibration absorber. For example, an ABH beam is installed on a primary structure in [58, 59], a circular plate with varying thickness is considered in [60, 61], while ABH pillars are added to a beam in [62]. Leveraging on this idea, we propose here a vibration absorber based on the VI-ABH concept, which combines ABH effect with impact nonlinearity in order to enhance its low-frequency behaviour, that can be attached to a primary structure for vibration mitigation. The device is first presented and numerically investigated in order to highlight the most important design parameters. A primary structure consisting of a honeycomb panel, is used numerically and experimentally in order to demonstrate the efficacy of the absorber. This structure has been selected for its large dimensions, its complicated interior design with the honeycomb, its intrinsic small structural damping, as well as for space applications where the passive control of lightly damped complicated panels is of prime importance. A special emphasis is put on the passive control of the response to shock. To demonstrate the efficiency of the vibration absorber in such a context, shock response spectrum (SRS) is defined and used. Such SRS analysis is very widely used in the field of aerospace engineering, with the ability to provide a comprehensive view of the highest accelerations over a broadband frequency range, and is thus a convenient indicator to estimate the harm of spacecraft structure under shocks. These shocks are often generated by pyrotechnic sources and anti-vibration protection against these broadband sources is difficult to design, particularly in a context where mass additions are very limited.

2. Modeling and design of the VI-ABH absorber

This section is devoted to the presentation of the vibration absorber, its numerical modeling as well as a parametric study in order to assess its efficacy and find the most critical design parameters.

2.1. Presentation of the absorber

The vibration absorber is composed of a circular plate with varying thickness implementing the ABH effect, together with an impact mass m that is connected to the center of the circular ABH by a slender beam. Fig. 1(a) shows a schematic view of the absorber in grey, mounted on a primary structure in magenta, while Fig. 1(b) depicts a picture of the experimental device that is detailed in Section 3. All applications considered in this article use a honeycomb panel with length L and width b as a hosting structure. The device is attached to the primary structure at location (x_a, y_a). Fig. 1 shows one impact mass, but up to three added impactors will be considered in the developments. Considering the slender beam mainly oscillates around its fundamental mode, the resulting impact device can be seen as a single-degree-of-freedom oscillator with mass m and stiffness k. The vibro-impacts on the ABH occur at x_c.

The vibration absorber takes over the principal characteristics of the VI-ABH defined and studied in [53–55], with the main difference that the same working principles are now

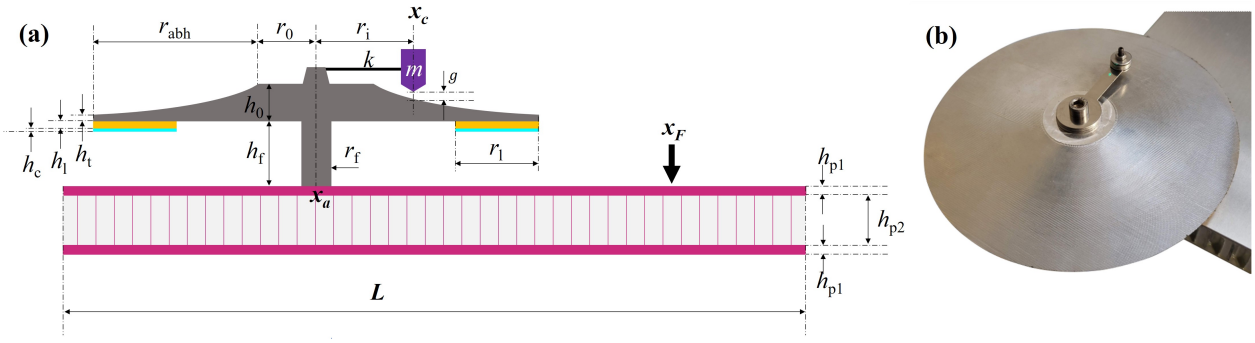

Fig. 1. VI-ABH vibration absorber. (a) Schematic view representing the absorber in grey, coupled to a primary structure in magenta. Important geometrical parameters defining the absorber and the primary structure are reported in the figure. The primary structure is a honeycomb panel with h_{p1} the thickness of the layers and h_{p2} the thickness of the core. The VI-ABH absorber is located at x_a, the size of the ABH region is r_{ABH}, with h_0 initial thickness, h_t terminal thickness, h_l and h_c the thickness of the viscoelastic layers. The vibro-impact is characterized by its mass m and the stiffness of the arm k. (b) Picture of the device mounted at one corner of a honeycomb panel.

integrated on an external device that can be mounted directly on a primary structure at a given location. It is thus awaited to recover the same qualities of the VI-ABH, which combines the efficiency of the ABH effect in the mid and high-frequency range, to a sharp and rapid energy transfer provided by the impacts. As an additional gain, the device is now more versatile and can be integrated easily to any host structure to passively damp out its vibrations. In order to understand and predict the main design parameters of the device, a numerical model is first developed in the next Section. Key design parameters appear obviously as being the tuning of the oscillation frequency of the impactors (through the mass m and stiffness k of the arm), the mobility and the gaps in between the different parts.

2.2. Modeling of the coupled system

The mechanical systems to be modelled, is composed of the primary structure (honeycomb panel), the vibration absorber which is a circular plate with varying thickness rigidly attached to the primary structure, and the impacting mass that is assumed to be correctly represented by a single oscillator equation with mass m and stiffness k. A 3D elastic finite element method (Structural mechanics COMSOL package) is used in order to space discretize the problem and to provide the modal parameters: eigenfrequencies ω_j and mode shapes $\phi_j(\mathbf{x})$, where $\mathbf{x}$ represents space, and modal damping ratios ξ_j are introduced via the imaginary part of the Young modulus. All the geometrical and material parameters are given in Tab. 1. From the FEM, a semi-discrete model is built based on the modal equations on which the added effects are integrated as: (i) the external excitation force with frequency content $p(t)$ and pointwise input location at $\mathbf{x}_F$, (ii) the vibro-impact oscillator with stiffness k and mass m with a contact force acting at point $\mathbf{x}_c$ and time content $f(t)$.

The displacement field of the coupled system is denoted as $u(\mathbf{x}, t)$, and is decomposed along the eigenmodes $\phi_j(\mathbf{x})$ following

$$u(\mathbf{x}, t) = \sum_{j=1}^{N_m} \phi_j(\mathbf{x}) q_j(t), \tag{1}$$

where $q_j(t)$ is the modal coordinate associated to mode j, and N_m is the total number of modes selected in the expansion. The eigenmodes are classically normalized with respect to mass. Let $u_a = u(\mathbf{x}_a, t)$ denote the displacement of the plate at the point where the absorber is located, and let $v(t)$ represent the temporal displacement of the impacting mass m. Then the equations of the coupled system and the impacting mass in the modal space read

$$\ddot{q}_j + 2\xi_j \omega_j \dot{q}_j + \omega_j^2 q_j = p(t)\phi_j\left(x_F\right) - f\phi_j\left(x_c\right) - k(u_a - v)\phi_j\left(x_a\right), \tag{2a}$$

$$m\ddot{v} = k(u_a - v) + f. \tag{2b}$$

The contact force $f(t)$ is modeled following a penalty approach with a Hertz-like law [53, 63]:

$$f(t) = k_c \left[u_c(t) - v(t) + g\right]_+^{\alpha}, \tag{3}$$

where k_c represents the contact stiffness and α the power-law dependence, $[\cdot]_+$ represents the positive part that is computed for the interpenetration η defined here as $\eta = u_c - v + g$, where $u_c = u(\mathbf{x}_c, t)$ is the structural displacement at the contact point and g is an initial gap that is set for the system at rest and represents the distance between the ABH circular plate and the impacting mass m in static position.

The ordinary differential equations of motion in modal space Eqs. (2) are then solved numerically. A special attention is devoted to dealing with the contact force, and a conservative scheme, designed to handle the penalty approach in modal space and derived in [63], is used. Let us conclude this section by giving the discrete equations that are solved at each time step for the time-marching scheme. To that purpose, the matrices $\mathbf{S}_F = [\phi_1\left(x_F\right),\ \phi_2\left(x_F\right),\ \cdots,\ \phi_{N_m}\left(x_F\right)]$, $\mathbf{S}_c = [\phi_1\left(x_c\right),\ \phi_2\left(x_c\right),\ \cdots,\ \phi_{N_m}\left(x_c\right)]$, and $\mathbf{S}_a = [\phi_1\left(x_a\right),\ \phi_2\left(x_a\right),\ \cdots,\ \phi_{N_m}\left(x_a\right)]$, defined as the modal components of the first N_m modes computed at locations x_F , x_c and x_a, are introduced. Thanks to Eq. (1), one writes easily the needed spatial displacements as

$$u\left(\mathbf{x}_i, n\Delta t\right) = \mathbf{S}_i \mathbf{q}^n, \quad \text{for} \quad i = F,\, c,\, a, \tag{4}$$

where the vector of nodal coordinates $\mathbf{q}^n$ at time n is used as

$$\mathbf{q}^n = \left[q_1\left(n\Delta t\right), q_2\left(n\Delta t\right),\ \cdots,\ q_{N_m}\left(n\Delta t\right)\right]^T. \tag{5}$$

For each time step n, the equation of motion for the system in Eq. (2) can be rewritten as:

$$\begin{aligned} &\mathbf{q}^{n+1} = \mathbf{C}\mathbf{q}^{n} - \tilde{\mathbf{C}}\mathbf{q}^{n-1} + \Delta t^2 \left[\mathbf{S}_F^T p^n - \mathbf{S}_c^T f^n - k\mathbf{S}_a^T(\mathbf{S}_a\mathbf{q}^{\mathbf{n}} - v^n)\right], \\ &m\ddot{v} = k\mathbf{S}_a^T(\mathbf{S}_a\mathbf{q}^{\mathbf{n}} - v^n) + f, \end{aligned} \tag{6}$$

where p^n and f^n are respectively the external and contact forces computed at time n. $\mathbf{C}$ and $\tilde{\mathbf{C}}$ are two diagonal matrices, whose entries are

$$C_{jj} = e^{-\omega_j \xi_j \Delta t}\left(e^{\omega_j\sqrt{\xi_j^2-1}\Delta t} + e^{-\omega_j\sqrt{\xi_j^2-1}\Delta t}\right), \quad \tilde{C}_{jj}{=}e^{-2\omega_j\xi_j\Delta t}. \tag{7}$$

The contact force is computed via

$$\mathbf{f}^{\mathbf{n}} = \frac{\psi(\eta^{n+1}) - \psi(\eta^{n-1})}{\eta^{n+1} - \eta^{n-1}}, \tag{8}$$

where the potential function describing the contact has been introduced as $\psi(x,t) = \frac{k_c}{\alpha+1}[\eta]_+^{\alpha+1}$. Thanks to the properties described in [63] and used for instance in [53], this choice of numerical scheme ensures that a discrete energy is conserved, providing interesting stability features for the numerical method. As for the vibro-impact parameters, they have been set to $k_c = 10^{11}\mathrm{N/m}^{1.5}$ and $\alpha = 1.5$, in order to ensure the rigidity of the contact, following previous studies [53, 54].

As a summary, the model is built upon the use of the FEM in order to derive the modal characteristics of the coupled system, from which the eigenfrequencies ω_k and the projection matrices $\mathbf{S}_a$, $\mathbf{S}_c$, $\mathbf{S}_F$ allowing one to go from physical space to modal space, are retrieved. The equations of motion are integrated in time using a time-marching conservative scheme that needs a Newton-Raphson procedure at each time step to solve the nonlinear equation.

2.3. Numerical Results and design rules

In this section, the performances of the proposed VI-ABH absorber are evaluated numerically, with the aim of performing a detailed parametric study to reveal the most salient features for an effective design. In order to carry out the analysis, the geometric and material parameters of the system are listed in Tab. 1, where the first column accounts for the geometric parameters (also given in Fig. 1(a)), and the second column is the material parameters. The primary structure is a honeycomb panel made of aluminium, with length L=800 mm, width b=600 mm, and total thickness $2h_{p1}+h_{p2}$=20 mm, including the thickness of the core h_{p2} and the thickness of both skin panels h_{p1}. The material parameters for the panel are referred to with a subscript 'p' in Tab. 1, including Young modulus E_p, material density ρ_p, loss factor η_p and Poisson ratio v_p. The circular ABH absorber is defined by its geometrical parameters r_f, h_f, r_0, r_{abh}, h_0, h_t, and material characteristics with subscript 'abh'. It is attached to the corner of the host panel with coordinate $[x_a, y_a] = [20, 20]$ mm. Finally, the added layers coated to the ABH are defined by their radius r_l. The visco-elastic damping layer is of thickness h_l with material characteristics denoted with the subscript 'l', and the constraint layer is of thickness h_c with material characteristics with subscript by 'c'.

Besides, for all the numerical simulations later on, the sampling frequency is selected as $f_s = 160$kHz and the time signals are calculated up to 10s. The number of modes N_m is set to 150, covering a frequency range from $f_1 = 166$ Hz to $f_{150} = 8.5$ kHz.

Tab. 1: List of parameters used in the numerical simulation

Geometric Parameters	value	Material Parameters	value
L	800 mm	E_p	70 Gpa
b	600 mm	ρ_p	2700 kg/m^3
h_{p1}	1.5 mm	η_p	0.012
h_{p2}	17 mm	v_p	0.3
r_f	5 mm	E_{abh}	70 Gpa
h_f	5 mm	ρ_{abh}	2700 kg/m^3
r_0	20 mm	η_{abh}	0.012
r_{abh}	60 mm	v_{abh}	0.3
h_0	4 mm	E_l	7 Mpa
h_t	0.2 mm	ρ_l	1000 kg/m^3
h_l	0.2 mm	η_l	0.4
h_c	0.07 mm	v_l	0.3
r_l	30 mm	E_c	270 Gpa
r_i	40 mm	ρ_c	1143 kg/m^3
$[x_a, y_a]$	[20, 20] mm	η_c	0.012

2.3.1. Finite element analysis for the linear characteristics

The linear eigenmodes of the coupled system are calculated using a finite element approach. Fig. 2(a) shows the mesh used for the computations. The complete system has been discretised using 3D elements, with particular attention to the tapered region of the ABH absorber, as well as its complex coupling with the host panel. The primary structure is treated using the Reissner theory, where an equivalent thickness, mass ratio and Young modulus are given to model the honeycomb panel as an equivalent rectangular plate. Convergence studies have been performed in order to ensure the reliability of the numerical model by checking the accuracy of the computed eigenfrequencies up to 10 kHz. As a result of this analysis, a refined mesh containing 226283 degrees of freedom (dofs), has been selected. Two different analyses have been processed. The first one is for the VI-ABH absorber alone, in order to understand its linear characteristics, reported in Fig. 2(b). Then the eigenmodes of the coupled system have been computed and reported in Fig. 2(c). In each of these two figures, the modal damping ratios are reported as a function of the eigenfrequencies, and some of the mode shapes are inserted in the plot. Structural damping has been taken into account in the FE analysis by introducing a complex Young modulus $E_i^* = E_i(1 + j\eta_i), \forall i =$ 'p', 'abh', 'l', 'c', following the properties E_i and η_i shown in Tab. 1.

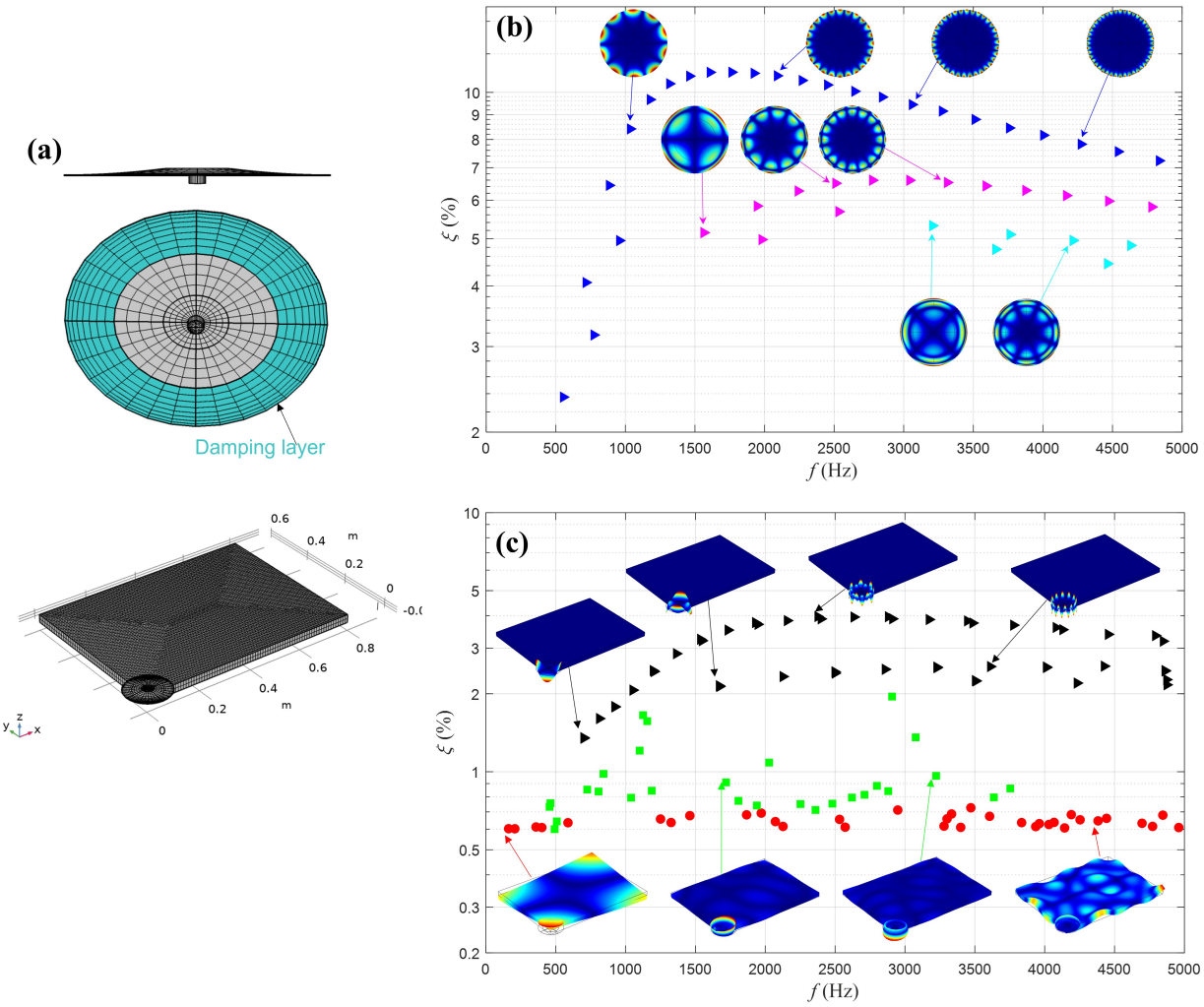

Fig. 2. Linear characteristics of the system, (a): Finite element model for the VI-ABH absorber alone and mounted on the honeycomb panel, (b): Eigenmode analysis for the VI-ABH alone, showing the modal damping ratio as a function of the eigenfrequencies, (c): Eigenmode analysis for the coupled system VI-ABH absorber + primary system.

In Fig. 2(b), the modes of the VI-ABH absorber have been grouped into three different types according to the number of nodal diameters of the eigenmode shapes. This grouping is meaningful since the representation of the modal damping ratio as a function of the eigenfrequencies makes clearly appear different branches of solutions that are more or less damped. Note that, due to the thickness decreasing, the nodal diameters are close to the edge of the circular plate. Modes with one nodal diameter are marked with pink triangles and can be distinguished from the modes without nodal diameters (blue triangles) and two nodal diameters (cyan triangles) by clearly inspecting the pattern at the edge.

The modes having the highest damping capacities are marked with blue triangles and

have no nodal diameter. They correspond to vibration modes where the energy is trapped in the ABH region and can be classified as hyper-damped modes. On the other hand, pink and cyan triangles represent modes having respectively one and two nodal diameters. Since involving also non-negligible vibrations of regions in the center of the circular plate, they are less damped. One can also observe that the first ABH mode involving localized vibrations is the one at 554 Hz. It is thus assumed that the cut-on frequency for this ABH design is around 500 Hz such that the ABH effect reaches its most efficiency for frequencies higher than 500 Hz. In the remainder of the analysis, we will thus refer to the low-frequency range as the frequencies that are below 500 Hz, while $f > 500$Hz will correspond to the high-frequency range. Based on this knowledge of the linear behaviour of the ABH, the impact mass will be added to the system in order to enhance vibration mitigation by transferring energy from the low to the high-frequency range.

Fig. 2(c) displays the eigenmodes of the coupled system, where the modal damping ratios are ranging in a large interval from 0.6% to 5%. Importantly, different solution branches can be highlighted, revealing different damping characteristics linked to specific vibratory features. In order to assess this more quantitatively, a coupling factor R is introduced and defined as:

$$R = E_{abh}/E_{tot}, \tag{9}$$

where E_{abh} is the kinetic energy in the ABH region and E_{tot} is the total kinetic energy. From this definition, the coupling factor R simply describes to what extent the vibration energy at a given mode is localized into the VI-ABH absorber, or more spatially distributed to the primary structure. Without loss of generality, three different mode families are defined and grouped according to the value of R. The first family corresponds to highly localized modes with $R > 0.9$ and are represented with black triangles in Fig. 2(c). This family contains the eigenmodes that are the most efficient for vibration damping thanks to the strong activation of the ABH effect. The second family is represented with green squares and is such that $0.1 < R < 0.9$. In this case, the damping of the host panel is improved by the presence of the absorber, but the coupling is not so efficient and the improvement is less significant. Finally, the red circles represent the uncoupled modes with $R < 0.1$. In this last family, the coupling between the primary structure and the absorber is not efficient and the damping ratio remains small, with a value that is close to the one given by considering only the structural losses of the honeycomb panel. Indeed, the damping ratio gives a value of 0.6% on average, equivalent to a loss factor of about 1.2% given in Tab. 1 for the panel alone.

2.3.2. Evidence of the energy transfer

In the design of the VI-ABH absorber, the aim of the mass m is to repeatedly impact the circular plate in order to rapidly transfer energy from the low to the high-frequency range thanks to the nonsmooth contact nonlinearity. This is illustrated in Fig. 3, which shows the frequency spectrum of the vibration at the point $\mathbf{x}_a$, corresponding to the foot point where the ABH absorber is located. The primary structure is here excited in the low-frequency range with a white noise restricted in the frequency range $[0,\ 500]$ Hz, below the cut-on frequency identified for the VI-ABH absorber. Two cases are shown, one case where the

vibro-impact is not present such that only the ABH effect (which is not effective in this frequency band) might damp out the vibration (blue curve); and a second case with a single mass m for vibro-impacts (red curve). For this simulation, no special care has been devoted to tune the parameters of the VI that have been set arbitrarily.

With the VI-ABH at hand, two clear distinctive features appear. First, a strong energy transfer is observed, which importantly contrasts with the case without impacts for frequencies over 500 Hz. Second, and as a consequence of the first point, the energy of the peaks present in the range [0, 500] Hz, have decreased. In this low-frequency range, three modes are present, the two prominent peaks corresponding to modes 1 and 3. The decrease of the vibrational energy in the first mode is the most impressive, with a loss of 10dB for the maximum. On the other hand, mode 3 is less affected, and mode 2 shows almost no change.

Since this result has been obtained without resorting to any tuning strategy, the next Section is devoted to a parametric analysis of the VI-ABH absorber main characteristics, in order to figure out the key parameters for an optimal tuning. The main parameters to be optimized are the mass m; the stiffness k, the gap g. Also, the case with multiple impact masses will be considered with different tuning rules in order to achieve the best possible scenario.

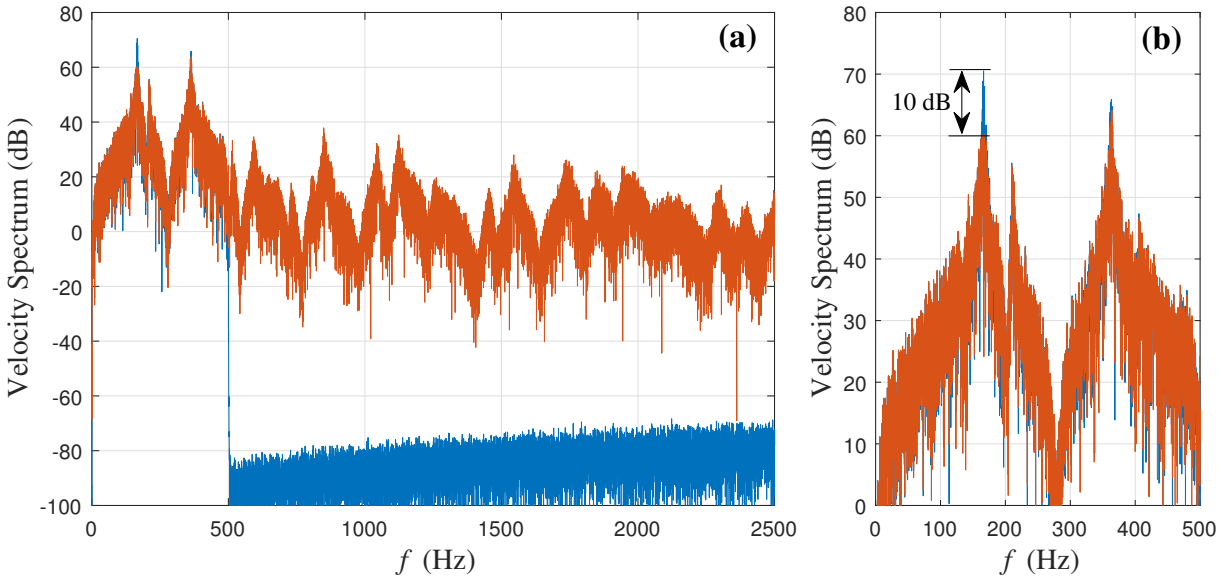

Fig. 3. Velocity spectrum response of a point selected on the circular plate, for two different cases for comparison. Blue: linear ABH absorber without impact mass. Red: nonlinear VI-ABH absorber with a single mass m=10 g. The primary structure is excited with a band-limited white noise in the frequency range $[0, 500]$ Hz. (a) Response in the range $[0, 2500]$ Hz. (b) Close-up view in the frequency range of the excitation to better appreciate the decrease of the main peaks.

2.3.3. Tuning the characteristics of the impactor

In order to evaluate quantitatively the energy transfer and peak reduction brought about by the vibro-impact, a performance indicator denoted by I_Ω is introduced as

$$I_\Omega = 10\log_{10}\left[\frac{\int_\Omega P_v^{\text{cur}}(\omega)d\omega}{\int_\Omega P_v^{\text{ref}}(\omega)d\omega}\right], \tag{10}$$

where $P_v^{\text{cur}}(\omega)$ and $P_v^{\text{ref}}(\omega)$ accounts for the velocity spectrum of the output velocity $v(\mathbf{x}_F, t)$ measured at the excitation point $\mathbf{x}_F$, while the superscripts 'cur' and 'ref' are used to denote the current case (with impacts in a configuration under study) which is compared to a reference case where impacts are not activated (and thus corresponding to the linear ABH effect only). Ω denotes the frequency range of interest.

The location of the contact point, which also defines the length r_i of the vibro-impactor arm, was optimised on the basis of previous studies carried out by the authors [53–55]. The choice of r_i is a compromise that takes into account the high flexibility required for the VI effect (implying a long arm) and the possible damage caused by impacts in the fragile area of the tip (implying a short arm).

The first parameters to be investigated for the tuning of the impactor are the mass m and the stiffness k, which are jointly studied by investigating the effect of the vibration frequency of the single dof system appended to the circular ABH, and defined as $f = \frac{1}{2\pi}\sqrt{k/m}$.

Fig. 4 shows the numerical results obtained by focusing on the low-frequency range where the improvement is awaited, while displaying the indicator I_Ω for four different frequency intervals. Figs. 4(a-b) reports the improvement obtained by modifying the frequency of the impactor f when the indicator is centered around the first and the third eigenfrequency f_1 and f_3. Since these peaks are the most prominent ones, see Fig. 3, it is logical to focus on the gains that can be awaited thanks to the reduction of these two. In each case, the frequency interval is defined by selecting a frequency band of width $0.2f_i$ in the vicinity of the considered frequency. For example, I_{f_1} is computed over the interval $[0.9f_1, 1.1f_1]$ Hz. Note that, in each case, the system is forced with a [5, 500]Hz white noise excitation at one of the corners (*i.e.* located at $\mathbf{x}_F$=$\mathbf{x}_a$), and three different amplitudes are tested: 2N, 20N and 50N. Finally, Figs. 4(c-d) reports the results obtained when considering the frequency range of the excitation [5, 500]Hz for the indicator, and the high-frequency range [500, 5000]Hz.

Figs. 4(a-b) reveal a strong dependence of the efficiency with respect to f, and highlights that the best improvement in terms of increased damping is obtained when the impactor's frequency is set at 100Hz for controlling mode 1 (with a maximum gain of almost 6dB with respect to the linear case without contact) and at 240Hz for mode 3. The value of 6dB is a bit less than the value reported in Fig. 3 (a maximum reduction of 10dB at mode 1 with $f = 100$ Hz), because the indicator here is computed on an interval instead of focusing on the maximum only. Nevertheless, the behaviour of the indicators reported in Figs. 4(a-b) clearly shows that it is sensitive to f and there is a clear minimum that can be reached. Outside the region of the minimum, the gain is marginal. Interestingly, the minimum is obtained in each case for a value which is slightly larger than $f_j/2$, where f_j refers to the eigenfrequency

of mode j, as ascertained by the red dotted lines in Figs. 4(a-b). For mode 1, the minimum is obtained for a value that is 20% larger than $f_1/2$, while for mode 2 it is 33%.

The main conclusion is that the tuning of the impactor's frequency is of prime importance in order to achieve vibration mitigation of the modes that are below the cut-on frequency. Note that to our knowledge, there are no theoretical explanations for this minimum value. A similar pattern and a demonstrated rule exist for the case of Nonlinear Energy Sink (NES) and vibro-impact dampers, see *e.g.* in [64–67], where the optimal damping is shown to be for two impacts per periods. Nevertheless, the case considered here is slightly different and needs further study to elaborate a proof. Fig. 4(c) highlights two minima when reporting the indicator on the low-frequency band [0,500]Hz, underlining that most of the vibrational energy is contained within modes 1 and 3. In the same line, it is observed in Fig.4(d) that the values for which the energy is most efficiently transferred to the high-frequencies, correspond to the minima found in the low-frequency range. As a last remark, it is clearly observed that the obtained results are not sensitive to the amplitudes tested, which however corresponds to a comfortable range from small to large excitations. Of course, a lower limit to the amplitudes exists, when the impacts are not triggered, but this lower value was not considered in this figure.

Now that the most important parameter (eigenfrequency of the added impact oscillator) has been studied, let us consider the other meaningful parameters, starting with the initial gap g. Fig. 5 summarizes the obtained results by focusing on the behaviour of two indicators, namely I_{f_1} and $I_{[0,\,500]}$, when the gap g is varied, and for the three amplitudes of forcing already tested: 2N, 20N and 50N. The forcing signal is still set as a low-frequency band-limited noise in the range $[5, 500]$ Hz. The general behaviour of the indicator shows that for large values of the gap g there is obviously no gain in vibration reduction. Hence the curve tends to a constant value at 0dB for large gaps. When the gap decreases, the contact nonlinearity comes into play and there is a sharp transition to an efficient gain in the overall damping of the device. This transition occurs sooner for larger amplitudes of external excitation. Note that those curves have been obtained for a tuning of the eigenfrequency of the impact oscillator at $f = 100$ Hz. The obtained results are logical and underline the added effect brought by the vibro-impact to the absorber. It is thus recommended for practical application to set a vanishing gap for better efficiency.

Let us now consider separately the mass m of the absorber in order to question the efficacy of the device as a function of its total weight, since the mass of a vibration absorber is a key feature. Moreover, two different cases are here analyzed by considering either a single added impact oscillators, or three of them. Note that for each configuration, the eigenfrequency of the oscillator is kept constant at 100 Hz by adjusting simultaneously the stiffness k; in order to target the best efficiency of the device in passively controlling the first eigenmode of the structure. Fig. 6 shows the numerical results obtained, again for the two most meaningful indicators I_{f_1} for the local performance around mode 1 in Fig. 6(a), and the overall performance $I_{[0,\,500]}$ in Fig. 6(b). The results clearly underline that an increasing total mass generally leads to a better vibration reduction performance, which is an awaited result. Note however that lightweight vibration absorbers are generally desirable meaning that a

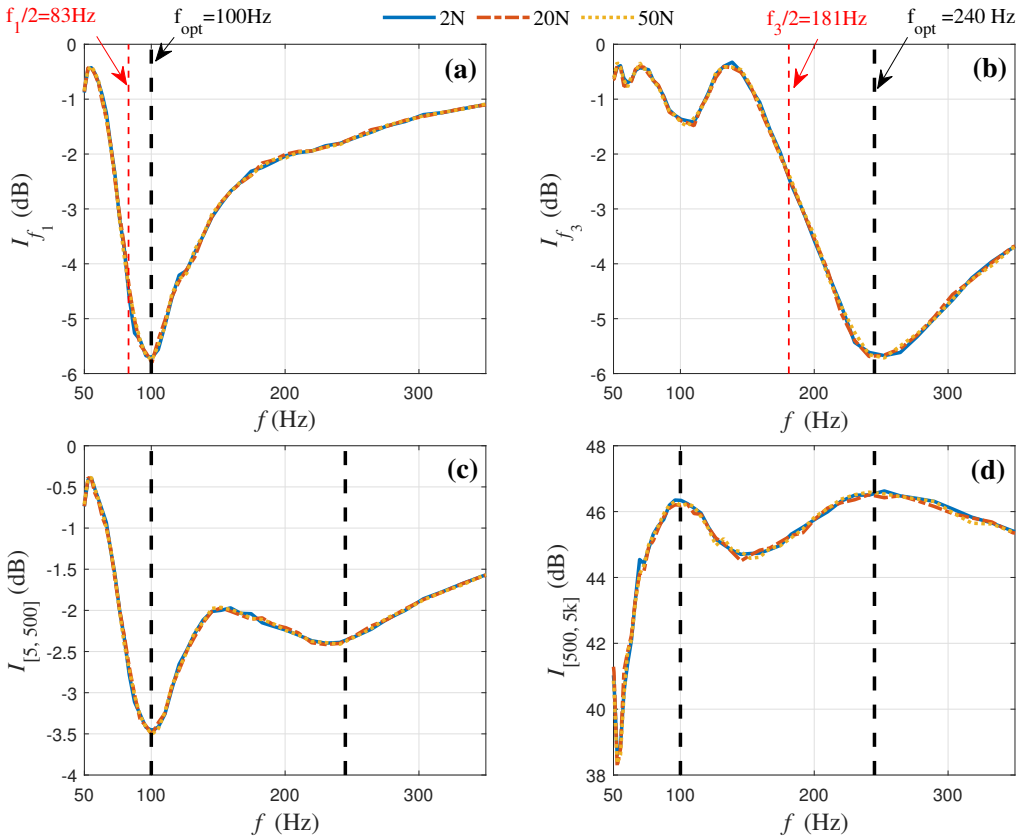

Fig. 4. Indicators I_f as a function of the oscillation frequency of the vibro-impactor. Results obtained under a white noise excitation centered in the low-frequency range [0, 500] Hz, and for three different amplitudes: 2N, 10N and 50N. (a) Indicator centered around the fundamental eigenfrequency of the system. (b) Indicator centered around mode 3. (c) Low-frequency range indicator. (d) High-frequency range indicator.

compromise must be found here. Comparing now the effect brought about by considering three added oscillators instead of a single one (with the same mass either concentrated in a single oscillator or distributed among the three), it is observed that the effect is small for the local performance quantified by I_{f_1}. On the other hand, the triple-mass configuration clearly outperforms the single-mass configuration when considering the overall low-frequency performance quantified by $I_{[0,\,500]}$. This effect is attributed to the more complex dynamics exhibited by the triple-mass configuration which in general leads to better energy transfer to the high-frequency range. As a conclusion, the results show that using multiple impacting devices is generally favourable and can provide better performance for multiple mode vibration reduction of the plates.

In order to further investigate the increase of performance brought about by considering three added vibro-impact oscillators, Fig. 7 summarizes the results obtained for 5 different configurations. Each configuration is described by a triplet of integer, where '111' means

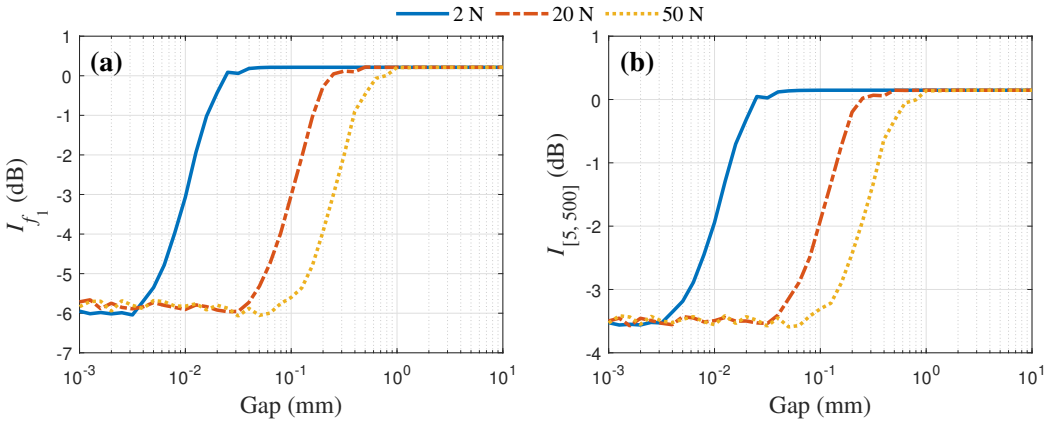

Fig. 5. Variations of two indicators as a function of the initial gap g. (a) I_{f_1} underlining the gain in efficacy around the fundamental mode, (b) low-frequency efficacy: $I_{[0,\,500]}$. Other parameters of the vibro-impact oscillator have been set to m=10 g, k=4000 N/m, resulting in a eigenfrequency f=100 Hz

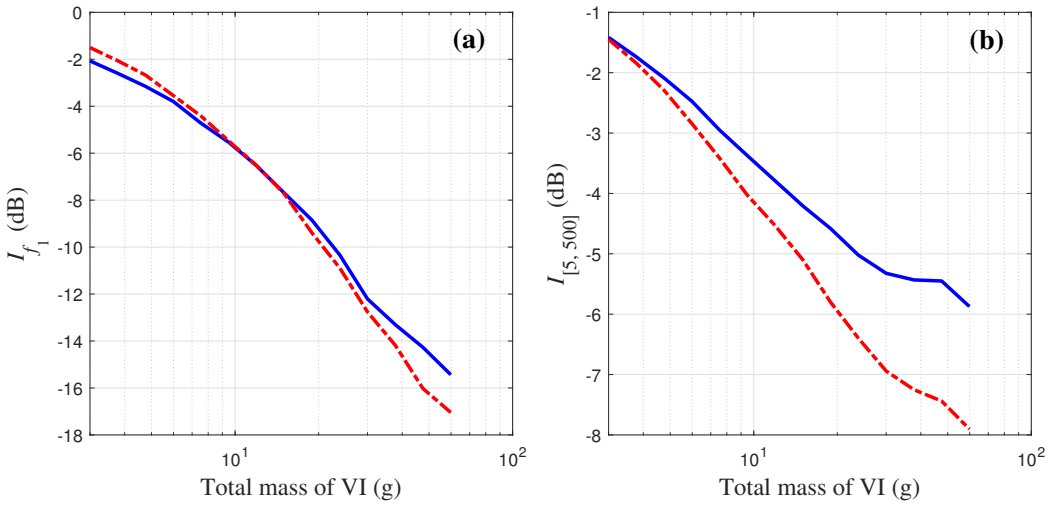

Fig. 6. Performance of the VI-ABH absorber as function of the impactor's mass. Blue solid curves: case with single mass configuration, red dash-dotted curves: case with triple mass configuration. (a) Variation of indicator I_{f_1}, (b) variation of indicator $I_{[0,\,500]}$. The stiffness k is varied accordingly to the mass m such that the eigenfrequency of the impacting system is kept constant at f=100 Hz.

for example that the three oscillators have been set to control mode 1 following the rule on the eigenfrequency found before, while '333' means that the three are tuned to control mode 3, and '113' means two oscillators optimized for mode 1 and 1 oscillator tuned to control mode 3. Fig. 7(a) shows the behaviour of four indicators: three local performance indicators on the targeted modes I_{f_1}, I_{f_2}, I_{f_3}, and one global low-frequency performance indicator $I_{[0,\,500]}$. Figs. 7(b-d) shows the velocity spectrum for three of the 5 configurations

tested ('111', '333' and '113'), in order to better assess the performances. Note that other configurations (*e.g.* '112' with two oscillators on mode 1 and one impactor on mode 2) have also been tested but are not reported in the figure since providing results that are not better. As awaited, configurations centered on a single mode, namely '111', '222, and '333', are the best configurations for the corresponding local performance indicator I_{f_1}, I_{f_2} and I_{f_3}. However the most meaningful being the global low-frequency indicator $I_{[0,\,500]}$, one can see that three configurations give with very good results, '111', '113' and '123'. This result underlines that it should be generally favourable to consider different tunings for the different added impact oscillators, in order to gain better control of the different modes that are below the cut-on frequency. In our configuration, mode 1 has the most prominent peak in the low-frequency range and needs to have special care, but of course, the conclusions drawn here should change for different primary structures, the general idea being to control the most important modes with targeted vibro-impact oscillators.

To summarize the numerical results, the introduction of the vibro-impact oscillator allows effective transfer of energy, which in turn reduces the low-frequency peaks of the primary structure. The peak reduction performance at a given mode is mainly related to the stiffness and mass of the impactor. The tuning of the optimal frequency has been found to be slightly larger than half the eigenfrequency of the mode to be controlled. Increasing the mass improves the vibration mitigation performance, but comes in opposition to the target of having a lightweight vibration absorber, such that a compromise must be found. The gap is recommended to be as small as possible. Finally, using multiple absorbers allows improving the performance by controlling more modes in the low-frequency range.

3. Experimental demonstration

3.1. Setup and signal processing

The setup of the experimental system is presented in Fig. 8. The primary structure is a rectangular honeycomb plate made of aluminium with dimension 800 mm × 600 mm × 20 mm, i.e. it has the same size as compared to the previous numerical investigation given in Tab. 1. It is hanged over a rigid frame so that its boundary conditions can be represented by free-free conditions. The VI-ABH absorber is attached to a corner of the host plate. One or two impactors can be used (see pictures in Fig. 8(b-c)). In order to thoroughly study the efficiency of the absorber, two types of excitation are considered. The first is a broadband white noise excitation performed with a shaker mounted on the plate, as shown in Fig. 8(d). The second one is a shock excitation generated by using a marble pendulum shown in Fig. 8(e). The pendulum is systematically released from the same position, which guarantees the repeatability of the shock conditions. The two types of excitation are applied to the point where the VI-ABH is fixed, as shown in Fig. 8(d-e). The VI-ABH thus absorbs the vibrations entering the plate by this single input point. Force and acceleration at the excitation point are measured by an impedance head (PCB 288D01). A vibrometer (Polytech PSV-500) is used to measure the velocity signals at any point of the panel or VI-ABH.

In the tested system, the mass of the ABH absorber is about 3% of the total mass of the host panel, which is still small. The modal damping of the host panel without the ABH

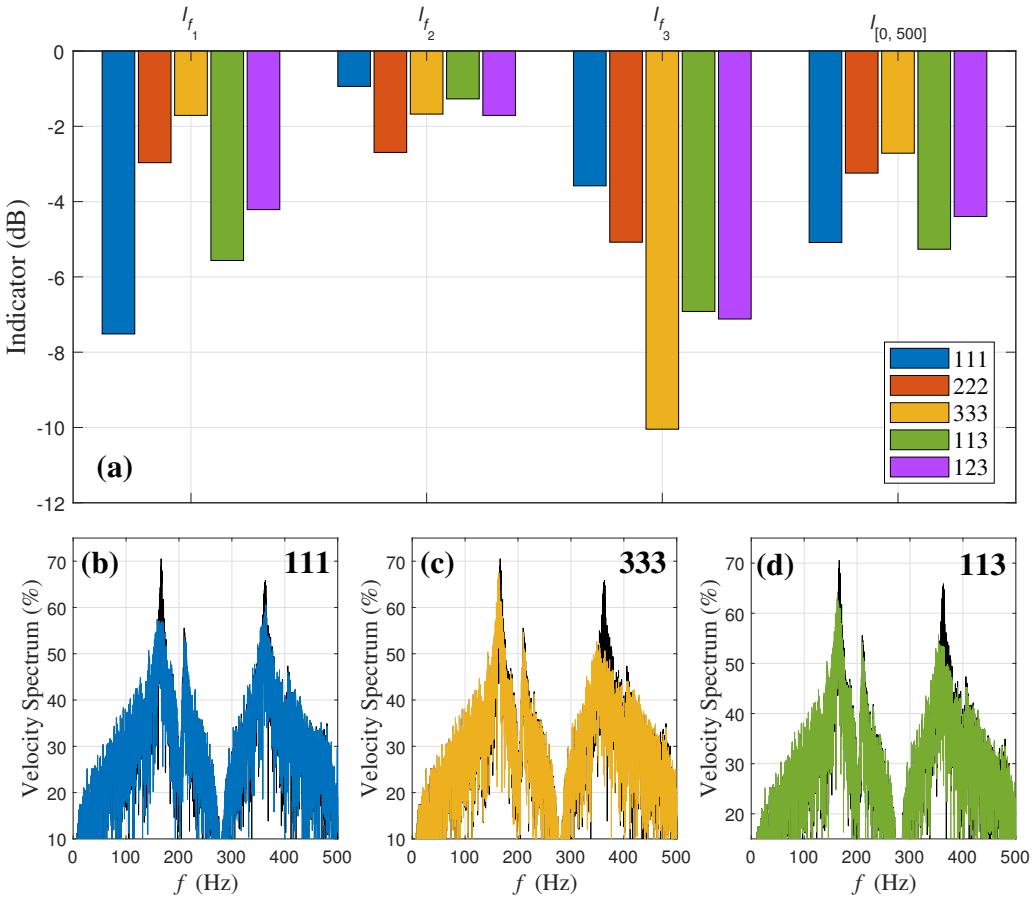

Fig. 7. Behaviour of the VI-ABH absorber with three added impact masses tuned differently in order to control multiple vibration modes in the low-frequency range. Five tested configurations: '111' for all three masses targeted to mode 1, '222' for all three masses targeted to mode 2, '333' for all three masses targeted to mode 3, '113' for two masses targeted to mode 1 and 1 mass targeted to mode 3, and '123' for each mass targeted to each mode. (b,c,d) Velocity spectrum recorded at point $\mathbf{x}_F = \mathbf{x}_a$ for three specific configurations: (b) '111', (c) '333' and (d) '113'. Other parameters have been set as: total mass 30g with 10g each and stiffness tuned to fit the targeting eigenfrequency, i.e. 100Hz for mode 1, 180Hz for mode 2, and 240Hz for mode 3.

absorber is measured and varies from 0.1 to 2%, with an average value of 0.66% in the frequency range [0, 5000] Hz. The mobilities of the panel and the ABH are shown in Fig. 9 when these two structures are isolated, i.e. decoupled from each other. In order to guarantee a strong coupling between these two structures, it is necessary to carry out an impedance matching and thus to make sure that the mobilities have the same orders of magnitude. As these mobilities vary with frequency, this condition is achieved on average over the frequency range of interest. The fact that these two mobilities are of the same order of magnitude is an important dimensioning rule for guaranteeing appropriate coupling between the ABH

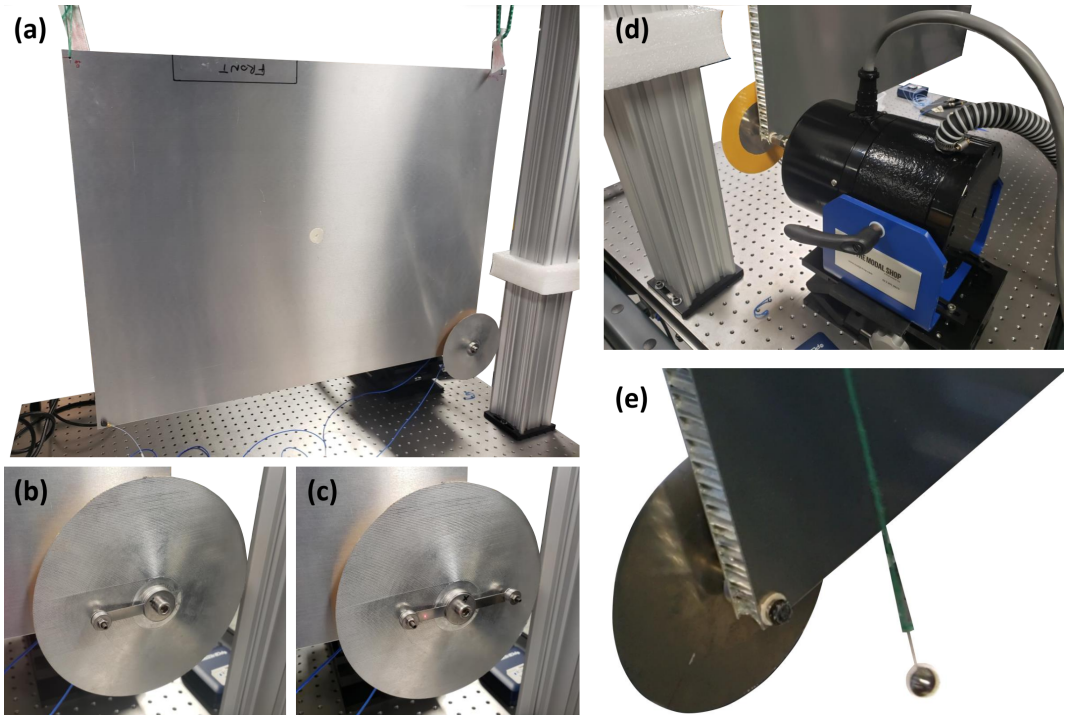

Fig. 8. (a) Experimental setup of the system showing the primary structure (hanged honeycomb panel); (b) close-up view of the VI-ABH with 1 VI; (c) ABH with 2 VIs; (d) Close-up view of the electrodynamic shaker for broadband excitation; (e) Marble pendulum for impact excitation.

attenuator and the panel.

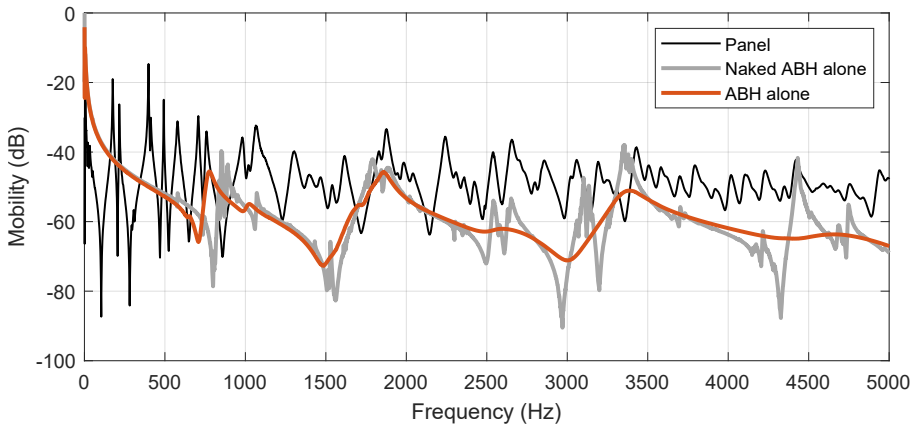

Fig. 9. Comparison of input mobilities between the host panel and the ABH attenuator. The measured input mobility of the panel alone, *i.e* without any coupling with the ABH is plotted in black. The mobility of the ABH attenuator without coating (naked ABH alone, *i.e.* uncoupled from the panel) is plotted in grey. In the presence of a coating, the mobility of the ABH attenuator (alone) is shown in red and is smoothed as compared to one of the naked ABH.

3.2. Performances in forced vibrations

The ability of the device to damp vibrations is first evaluated in a forced regime. The performance is estimated using the ratio between the velocity spectrum and the force spectrum at the excitation point. The modulus of this ratio corresponds to the modulus of the mobility of the structure when linear vibrations are assumed. In the presence of non-linearities induced by vibro-impacts, the indicator no longer corresponds to the modulus of a transfer function but allows evaluation of the performance of the attenuator. By abuse of language and convenience, this indicator will also be called *mobility*.

Figure 10 (a) and (b) shows the mobility of the system in 3 different configurations: the mobility of the panel alone (blue curve) reveals the presence of many resonant peaks over a wide range of frequencies. The coupling of the panel with a linear ABH, introduces an added dissipative mechanism (orange curve in Fig. 10(a)), which results in some smoothing of the resonance peaks in the high-frequency range (above 1kHz). This effect is the one classically expected for linear ABH. We also observe in Fig. 10(a) that the mobility of the panel/ABH coupled system is also decreased on average, especially in the high-frequency range, which is the consequence of an increase in the mass of the system.

The third case shown is that of a VI-ABH absorber with two impact masses that are respectively tuned in order to control mode 1 and mode 2. Following the design rules found in the numerical study, the eigenfrequencies of the impactor systems have thus been set at half the eigenfrequencies of modes 1 and 2, respectively. This configuration is denoted as 'ABH+2VI@f1+f2' in the figure. Note that for the sake of simplicity, the tuning has been set experimentally to half the eigenfrequency in order to avoid repetitive experiments for finding the optimal value, which was found numerically at a value slightly larger than $f/2$. Nevertheless, the robustness of this fine-tuning is illustrated after, see Fig. 12.

Fig. 10(a-b) shows that the mobility peaks of the VIs@f1+f2 system (green curve) are severely reduced as compared to the case without impacts, underlining the important gain brought about by this added device and the introduction of an important, nonsmooth nonlinearity. This demonstrates experimentally the efficacy of the energy transfer to the high-frequency range induced by the impacts and the efficacy of the vibration damping at high frequencies induced by the ABH effect. Fig. 10(b) highlights the important gains obtained in the low-frequency range, where the effect of the impacts is to severely reduce the resonant peaks. Interestingly, even though the VIs have been tuned in order to control modes 1 and 2, a very efficient control of mode 3 is observed with a very important decrease of the peak by about 12dB for mode 3. On the other hand, the decrease for mode 2 is less important, underlining that a better tuning might be found. Nevertheless, the two prominent peaks corresponding to modes 1 and 3 have been severely decreased, showing the efficacy and versatility of the system that is able to control different peaks in the low-frequency range.

Fig. 11 shows a summary of the performances of all the tested configurations, including the one illustrated in Fig. 10, and other configurations such as 'ABH+1VI@f1' (single impact mass tuned at half the eigenfrequency of mode 1) and 'ABH+2VI@f1' (two impact masses, both tuned in order to control mode 1 so having exactly the same design, in order to study the cumulative effects of more impacting masses). Also, both the naked ABH (without

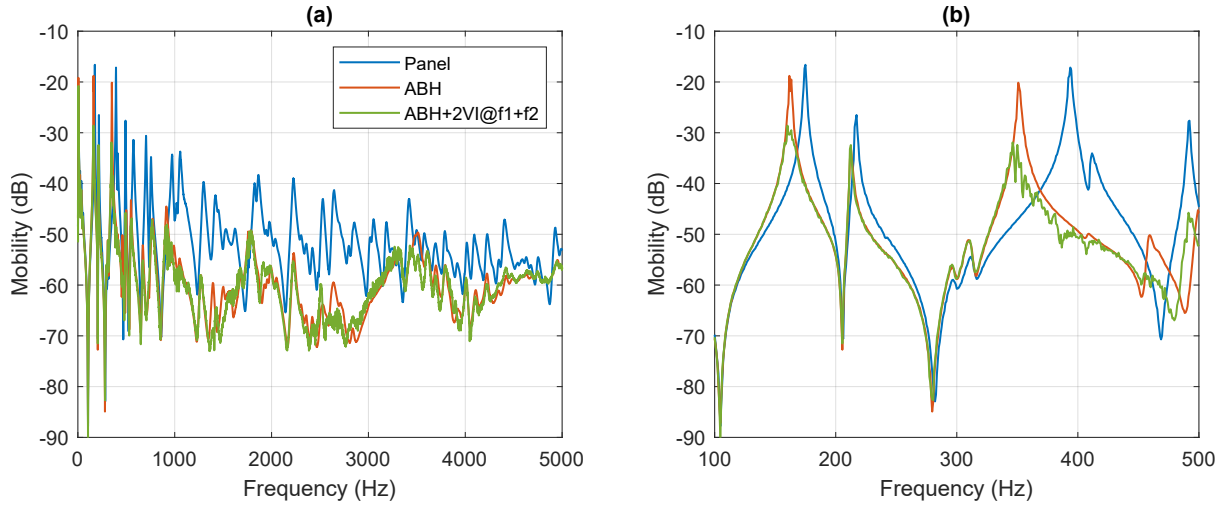

Fig. 10. (a) Input mobility of panel with ABH attenuator and vibro-impactors; (b) Zoom on mobility of first 3 resonances.

coated layers) and ABH configuration (with viscoelastic layers) are considered in order to highlight the gain that can be awaited by considering the impacting system embedded in the absorber. The attenuation indicators are calculated from experimental data on narrow frequency intervals $[0.9f_i, 1.1f_i]$ or on broad frequency bands [10-500]Hz, [500-5000]Hz, [10-5000]Hz, following the calculation used in the numerical study, see Eq. (10).

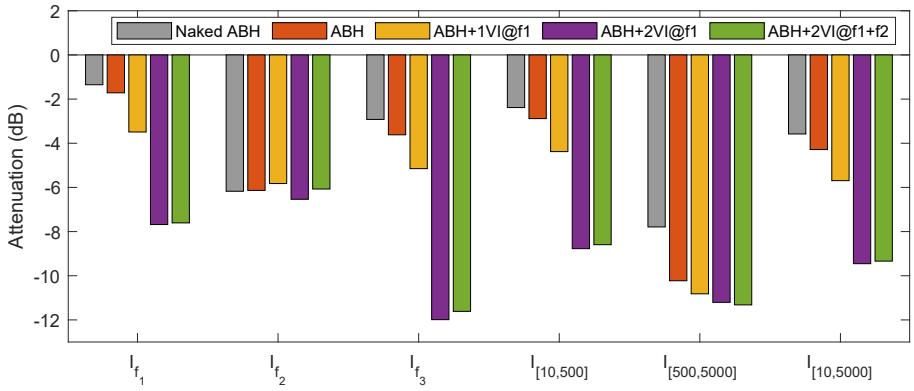

Fig. 11. Attenuation indicators for some tested configurations. The indicators at resonance frequency f_i are calculated on the interval $[0.9f_i, 1.1f_i]$.

The results show that the VI-ABH systems always give rise to better attenuation than the linear naked or coated ABH. It clearly demonstrates the relevance of considering vibro-impacts. The effect of the tuning of the vibro-impactor is clearly visible: for example, the attenuation around the frequency f1 (indicator I_{f1}) is significantly larger for ABH+2VIs@f1 than for the linear ABH. The same is observed around mode 3 where an important gain is observed by considering either 2 VIs tuned at $f_1/2$, or two VIs respectively tuned at

$f_1/2$ and $f_2/2$, following the discussion reported for Fig. 10. On the other hand, such an improvement of vibro-impact is currently not observable for mode 2 due to the fact that in the current set-up, the VI-ABH is located close to the node of mode 2, thus not efficiently coupled to the second mode of the primary structure. Other locations of the absorber should be reconsidered in order to gain better efficacy on mode 2. Nevertheless, since mode 2 is less energetic, the results show that very efficient control of the dominant modes can be obtained, with the good surprise that a non-targeted mode by design can be shown to be effectively controlled in the experiment, showing the versatility of the absorber. Focusing on the indicator $I_{[10,500]}$ which gives the most important information on the low-frequency control, and on $I_{[10,5000]}$ which highlights the broadband efficacy, it is observed that the two configurations with two VIs give the best results with important gains around 9dB.

In order to evaluate more properly the sensitivity of the device with respect to the design rules and the selection of the frequency of the impactor system, an experimental study has been conducted by considering 4 different tunings. The results are reported in Fig. 12. The first case is a tuning following the rule of half the frequency of the targeted mode. In this study, we focus on the first mode and the configuration where the impactor is exactly tuned at $f_1/2$ is denoted as '1VI@f_1' in Fig. 12. Three other configurations are tested where this half frequency has been decreased by 7 Hz, and increased by respectively 3 Hz and 18 Hz. They are respectively denoted as '1VI@f_1-7Hz', '1VI@f_1+3Hz' and '1VI@f_1+18Hz'. Fig. 12(a) shows the measured mobility in the frequency band of interest relative to the tuning of the impactor, highlighting how the four different tested cases are either exactly tuned at $f_1/2$, or slightly detuned.

The efficacy is assessed by the indicators reported in Fig. 12(b). The tuned case '1VI@f_1' is common to results reported in Fig. 11. The three detuned cases clearly underline that better efficacy can be obtained. In particular, the best case scenario for locally controlling mode 1 and quantified by I_{f_1} is that of the largest positive detuning. This result is in line with the numerical one reported in Fig. 4, which already underlined that the best tuning is obtained for a frequency that is slightly above $f_1/2$. Focusing on the indicator $I_{[10,500]}$ which accounts for the gains in the low-frequency range, one can observe again that a better attenuation is obtained with a case detuned to positive frequency. The gain is moderate also underlining the robustness of the device to frequency detuning. As a remark, the interested reader is also referred to the existing literature on vibro-impact NES where the variations of the performances have also been deeply investigated, see *e.g.* [68, 69] for recent experimental reports, and [10, 13, 64–67] for numerical, analytical and experimental studies.

3.3. Performances with shock excitation

The capability of the system to absorb the vibrations resulting from a shock is an important characteristic; one can even consider that the design of the absorber was conceived for this type of excitation. Three cases are considered: first, the panel alone is hit by the marble pendulum and its acceleration is recorded. Then the same experiment is repeated for the panel with the ABH mounted, and finally with the VI-ABH absorber, in the configuration where two impacting masses have been added, tuned respectively at half the frequency of

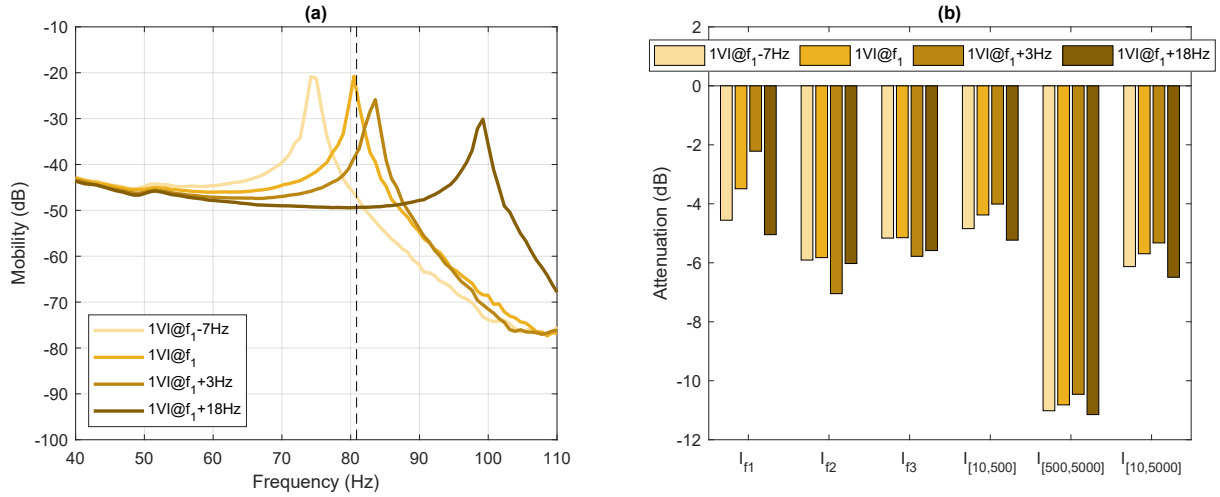

Fig. 12. Robustness to tuning accuracy of vibro-impactors. (a) Free mobility of vibro-impactors compared with the host panel mobility. The black dashed line represents the target tuning frequency of $f_1/2 = 81$ Hz. (b) Attenuation indicators for each tuning. The indicators at f_i are calculated on the interval $[0.9f_i, 1.1f_i]$.

mode 1 and mode 2 (and thus denoted as ABH+2VIs@f1+f2). Fig. 13(a) shows the recorded accelerations in time, while their spectrograms are shown in Fig. 13(b,c,d). From the temporal acceleration, the gain is obvious with an impressive decrease of the maximum acceleration (divided by a factor 3) at the first impact, underlining the ability of the absorbers to rapidly dampen out the vibrations on very short time scales. The VI-ABH shows a slightly better control than the ABH alone for mitigating the first temporal peak. This is also evidenced in the spectrograms, which highlight how the VI-ABH more effectively controls the first two peaks by redistributing the energy all along the spectrum.

To provide a more quantitative analysis, an energy decay indicator is introduced as

$$E_\sigma(\tau) = \frac{\int_\tau^{T_f} V^2 \, \mathrm{d}t}{\int_0^{T_f} V^2 \, \mathrm{d}t}, \quad \forall\, \tau \in [0,\ T_f], \tag{11}$$

where V is the measured velocity of the panel at the point x_F. The energy decay E_σ is the ratio between the energy of the signal computed between the current time τ and the end of the signal window divided by the total energy of the signal. For $\tau = 0$, $E_\sigma = 1$, and the decrease of $E_\sigma(\tau)$ allows comparing the fastness of energy absorption in each measured configuration.

Fig. 14 compares the energy decay for the cases with or without vibro-impact, it is clearly observed that with the presence of vibro-impact nonlinearities, the energy decay can be much faster as compared to the linear cases without vibro-impacts. More precisely, the energy decay time to 1% reduces from almost 0.8 s to less than 0.4 s.

Fig. 15 shows how the different strategies for defining the device compare on the indicator

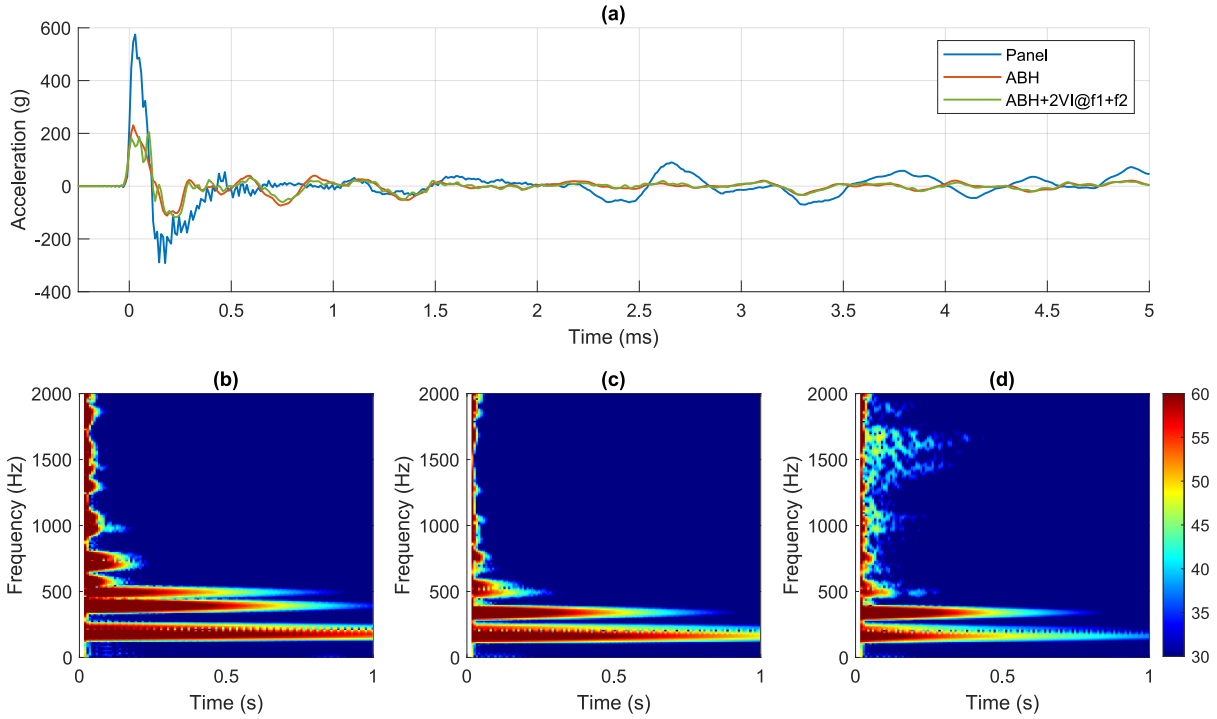

Fig. 13. (a) Acceleration time signals for three cases under study: panel alone (blue), panel+ABH (brown) and panel + VI-ABH with two added impact masses tuned at half the frequencies of mode 1 and mode 2. (b-d) Spectrograms of the acceleration signals shown in (a). (b) panel alone, (c) panel + ABH, (d) panel + VIABH.

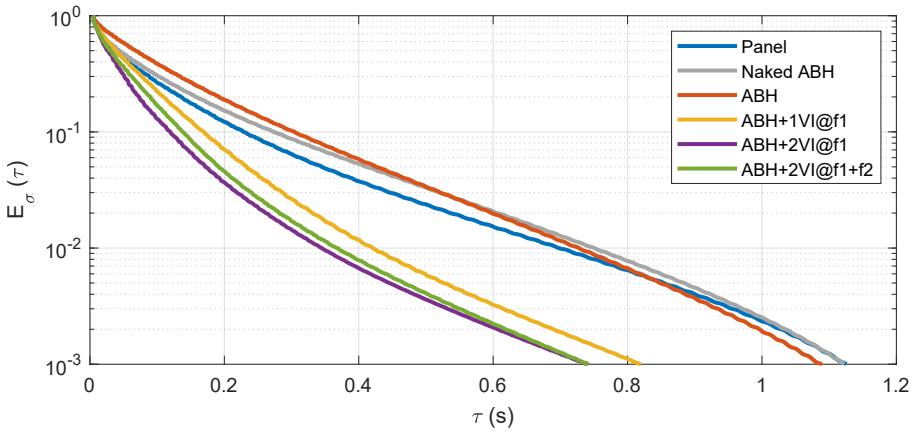

Fig. 14. Energy decay time for all the tested configurations.

SRS (Shock Response Spectrum), which is broadly used in the aerospace industry in order to evaluate the potential damage for the primary structure under transient shocks. Referring to [70–72], the SRS is defined as the maximal absolute acceleration response (in time) of a hypothetical single-degree-of-freedom oscillator, when it is forced at its base by the transient

acceleration input under analysis. It shows graphically how an oscillator would respond in time (in terms of peak acceleration) to the shock under study. To draw such a SRS curve, a fixed value for the quality factor $Q = 1/2\xi$ of the oscillator is set (in the present case, $\xi = 0.05$). The base signal taken as input to force the oscillator is the acceleration $\ddot{x}(t)$ recorded at the corner point of the panel in the Marble pendulum experiment shown in Fig. 8. Then as a final stage, the response acceleration $\ddot{y}(t)$ of the oscillator for varying values of its eigenfrequency f is computed, and the peak acceleration in time is recorded giving rise to a point at frequency f in Fig. 15. The calculation is repeated for each frequency f covering the range of interest.

Observing the result of this analysis reported in Fig. 15, it is seen that in the high-frequency range, all the curves with absorbers are well below the one of the naked panel, showing the efficiency of the ABH devices. This is due to the common advantage of linear ABH and VI-ABH in high frequencies. Moreover, in the low-frequency range around 160Hz (corresponding to the first eigenmode of the panel), it can be further observed that the peaks show an increased reduction for all the nonlinear cases (ABH+1VI@f1,ABH+2VI@f1, ABH+2VI@f1+f2), as compared to the other linear cases, meaning that the damage potential of the panel is well controlled. A comparison of the SRS for all the devices shows the ability of the ABH+2VI@f1 (purple curve) and the ABH+2VI@f1+f2 (green curve) to reduce the peak acceleration in the low-frequency range.

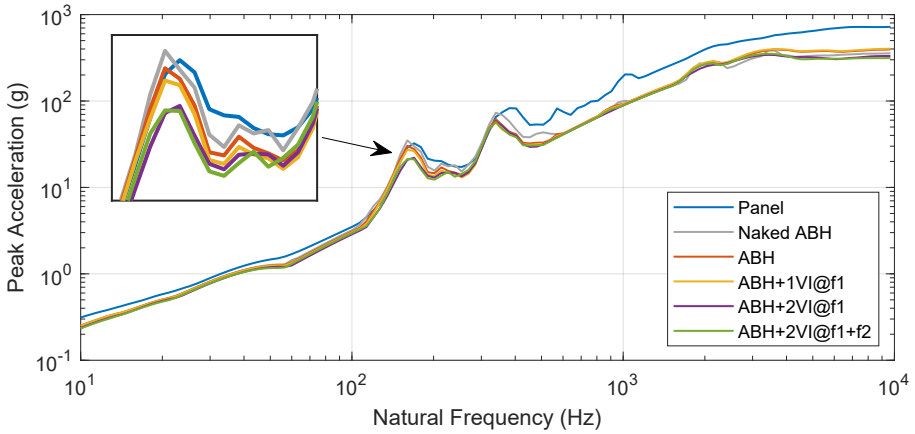

Fig. 15. Shock response spectrum (SRS) for different configurations of absorbers attached to the primary structure. A zoom on the first panel resonances at $160Hz$ is shown and demonstrates the advantages of the ABH+2VI@f1 (purple curve) and the ABH+2VI@f1+f2 (green curve) in the low-frequency range.

4. Conclusion

In this contribution, a novel broadband vibration absorber combining the acoustic black hole effect with vibro-impact nonlinearity is proposed. It is designed as a separate device that can be set to a primary structure in order to dampen its vibration, in the spirit of a classical tuned vibration absorber and in contrast to general implementations of the ABH effect that are embedded in the system. Comprehensive numerical and experimental analysis is hence conducted, in order to evaluate the vibration damping performance of the proposed absorber. A special emphasis has been put on low-frequency shock vibration absorption.

It is found that by taking advantage of the vibro-impact nonlinearity, the proposed VI-ABH absorber can effectively transfer the low-frequency energy to high frequency, and hence can be effective in a broadband manner including the low-frequency, that is commonly not able in a traditional ABH. In order to have optimal vibration suppression performance, the VI-ABH key design rule is in the tuning of the stiffness and gap of the associated mass. The eigenfrequency of the impact mass should be slightly above half the frequency of the targeted mode, and the gap needs to be selected as small as possible. By using multiple impact masses, each of them tuned to different targeted frequencies, an effective suppression for multi-mode vibrations in the low-frequency range can be achieved.

The results regarding the shock response spectrum and energy decay clearly underline that the proposed absorber performs excellently for controlling shock vibrations.

Acknowledgments

The authors are grateful to Julien Nicolas, from ENSIM Engineering School, who manufactured the ABH sample beam and to Mathieu Sécail and Félix Foucart for their help with the experiments and for helpful discussions.

Funding

This work was funded by the CNES (Centre National d'Etude Spatial) and the ANR French Agency through the FullFields lab program (No. ANR-17-LCV2-0010) joint with ACOEM company.

Conflict of interest

The authors declare that they have no conflict of interest.

References

[1] J.P. Den Hartog. *Mechanical Vibrations*. McGraw-Hill, New-York, 1934.

[2] O.V. Gendelman, L.I. Manevitch, A.F. Vakakis, and R.M. Closkey. Energy pumping in nonlinear mechanical oscillators, I: dynamics of the underlying Hamiltonian systems. *Journal of Applied Mechanics*, 68(1):34 – 41, 2001.

[3] A.F. Vakakis, L.I. Manevitch, O.V. Gendelman, and L. Bergman. Dynamics of linear discrete systems connected to local, essentially non-linear attachments. *Journal of Sound and Vibration*, 264(3):559–577, 2003.

[4] A. F. Vakakis, O. V. Gendelman, and et al. L. A. Bergman. *Nonlinear Targeted Energy Transfer in Mechanical and Structural Systems*. Springer, series: Solid Mechanics and its Applications. Springer, 2009.

[5] D. M. Egle. An Investigation of an Impact Vibration Absorber. *Journal of Engineering for Industry*, 89(4):653–657, 1967.

[6] I. López, J.M. Busturia, and H. Nijmeijer. Energy dissipation of a friction damper. *Journal of Sound and Vibration*, 278(3):539–561, 2004.

[7] G. Habib, T. Detroux, R. Viguié, and G. Kerschen. Nonlinear generalization of Den Hartog's equal–peak method. *Mechanical systems and signal processing*, 52 - 53, 2015.

[8] G. Habib and F. Romeo. The tuned bistable nonlinear energy sink. *Nonlinear Dynamics*, 89(1):179–196, 2017.

[9] F. Romeo, G. Sigalov, L.A. Bergman, and A.F. Vakakis. Dynamics of a linear oscillator coupled to a bistable light attachment: numerical study. *Journal of Computational and Nonlinear Dynamics*, 10(1), 2015.

[10] E. Gourc, G. Michon, S. Seguy, and A. Berlioz. Targeted energy transfer under harmonic forcing with a vibro-impact nonlinear energy sink: analytical and experimental developments. *Journal of Vibration and Acoustics*, 137(3):031008, 2015.

[11] S. Benacchio, A. Malher, J. Boisson, and C. Touzé. Design of a Magnetic Vibration Absorber with tunable stiffnesses. *Nonlinear Dynamics*, 85:893 – 911, 2016.

[12] P. Soltani and G. Kerschen. The nonlinear piezoelectric tuned vibration absorber. *Smart Materials and Structures*, 24(7):075015, 2015.

[13] G. Pennisi, C. Stephan, E. Gourc, and G. Michon. Experimental investigation and analytical description of a vibro–impact NES coupled to a single–degree–of–freedom linear oscillator harmonically forced. *Nonlinear Dynamics*, 88(3):1769 – 1784, 2017.

[14] O. Thomas, J. Ducarne, and J.-F. Deü. Performance of piezoelectric shunts for vibration reduction. *Smart Materials and Structures*, 21(1):015008, 2011.

[15] Z. A. Shami, C. Giraud-Audine, and O. Thomas. A nonlinear piezoelectric shunt absorber with a 2:1 internal resonance: Theory. *Mechanical Systems and Signal Processing*, 170:108768, 2022.

[16] M.A. Mironov. Propagation of a flexural wave in a plate whose thickness decreases smoothly to zero in a finite interval. *Soviet Physics Acoustics-USSR*, 34(3):318–319, 1988.

[17] V.V. Krylov and F.J.B.S. Tilman. Acoustic 'black holes' for flexural waves as effective vibration dampers. *Journal of Sound and Vibration*, 274(3-5):605–619, 2004.

[18] V.B. Georgiev, J. Cuenca, F. Gautier, L. Simon, and V.V. Krylov. Damping of structural vibrations in beams and elliptical plates using the acoustic black hole effect. *Journal of sound and vibration*, 330(11):2497–2508, 2011.

[19] L. Tang, L. Cheng, H. Ji, and J. Qiu. Characterization of acoustic black hole effect using a one-dimensional fully-coupled and wavelet-decomposed semi-analytical model. *Journal of Sound and Vibration*, 374:172 – 184, 2016.

[20] D.J. O'Boy, V.V. Krylov, and V. Kralovic. Damping of flexural vibrations in rectangular plates using the acoustic black hole effect. *Journal of Sound and Vibration*, 329(22):4672–4688, 2010.

[21] V. Denis, A. Pelat, F. Gautier, and B. Elie. Modal overlap factor of a beam with an acoustic black hole termination. *Journal of Sound and Vibration*, 333(12):2475–2488, 2014.

[22] K. Hook, J. Cheer, and S. Daley. A parametric study of an acoustic black hole on a beam. *The Journal of the Acoustical Society of America*, 145(6):3488–3498, 2019.

[23] M.R. Shepherd, C.A. McCormick, S.C. Conlon, and P.A. Feurtado. Modeling and optimization of acoustic black hole vibration absorbers. *The Journal of the Acoustical Society of America*, 141(5):4034–4034, 2017.

[24] L. Tang and L. Cheng. Enhanced acoustic black hole effect in beams with a modified thickness profile and extended platform. *Journal of Sound and Vibration*, 391:116 – 126, 2017.

[25] O. Aklouche, A. Pelat, S. Maugeais, and F. Gautier. Scattering of flexural waves by a pit of quadratic profile inserted in an infinite thin plate. *Journal of Sound and Vibration*, 375:38–52, 2016.

[26] J.Y. Lee and W. Jeon. Exact solution of Euler-Bernoulli equation for acoustic black holes via generalized hypergeometric differential equation. *Journal of Sound and Vibration*, 452:191–204, 2019.

[27] V.V. Krylov and R.E.T.B. Winward. Experimental investigation of the acoustic black hole effect for flexural waves in tapered plates. *Journal of Sound and Vibration*, 300(1-2):43–49, 2007.

[28] V. Denis, F. Gautier, A. Pelat, and J. Poittevin. Measurement and modelling of the reflection coefficient of an acoustic black hole termination. *Journal of Sound and Vibration*, 349:67–79, 2015.

[29] E.P. Bowyer, D.J. O'Boy, V.V. Krylov, and F. Gautier. Experimental investigation of damping flexural vibrations in plates containing tapered indentations of power-law profile. *Applied Acoustics*, 74(4):553–560, 2013.

[30] P.A. Feurtado and S.C. Conlon. An experimental investigation of acoustic black hole dynamics at low, mid, and high frequencies. *Journal of Vibration and Acoustics*, 138(6):061002, 2016.

[31] C. Zhao and M. G. Prasad. Acoustic black holes in structural design for vibration and noise control. *Acoustics*, 1(1):220–251, 2019.

[32] A. Pelat, F.Gautier, S.C. Conlon, and F. Semperlotti. The acoustic black hole: A review of theory and applications. *Journal of Sound and Vibration*, 476:115316, 2020.

[33] H. Zhu and F. Semperlotti. Two-dimensional structure-embedded acoustic lenses based on periodic acoustic black holes. *Journal of Applied Physics*, 122(6):065104, 2017.

[34] L. Tang and L. Cheng. Ultrawide band gaps in beams with double-leaf acoustic black hole indentations. *The Journal of the Acoustical Society of America*, 142(5):2802–2807, 2017.

[35] J. Deng, L. Zheng, and N. Gao. Broad band gaps for flexural wave manipulation in plates with embedded periodic strip acoustic black holes. *International Journal of Solids and Structures*, 224:111043, 2021.

[36] H. Ji, Y. Liang, J. Qiu, L. Cheng, and Y. Wu. Enhancement of vibration based energy harvesting using compound acoustic black holes. *Mechanical Systems and Signal Processing*, 132:441–456, 2019.

[37] J. Deng, O. Guasch, L. Zheng, T. Song, and Y. Cao. Semi-analytical model of an acoustic black hole piezoelectric bimorph cantilever for energy harvesting. *Journal of Sound and Vibration*, 494:115790, 2021.

[38] H. Li, O. Doaré, C. Touzé, A. Pelat, and F. Gautier. Energy harvesting efficiency of unimorph piezoelectric acoustic black hole cantilever shunted by resistive and inductive circuits. *International Journal of Solids and Structures*, 238:111409, 2022.

[39] J. Y. Lee and W. Jeon. Vibration damping using a spiral acoustic black hole. *The Journal of the Acoustical Society of America*, 141(3):1437–1445, 2017.

[40] S. Park, M. Kim, and W. Jeon. Experimental validation of vibration damping using an archimedean spiral acoustic black hole. *Journal of Sound and Vibration*, 459:114838, 2019.

[41] N. Gao, Z. Wei, H. Hou, and A. O. Krushynska. Design and experimental investigation of V-folded beams with acoustic black hole indentations. *The Journal of the Acoustical Society of America*, 145(1):EL79–EL83, 2019.

[42] T. Zhou and L. Cheng. Planar swirl-shaped acoustic black hole absorbers for multi-directional vibration suppression. *Journal of Sound and Vibration*, 516:116500, 2022.

[43] J. Deng, O. Guasch, and L. Zheng. Ring-shaped acoustic black holes for broadband vibration isolation in plates. *Journal of Sound and Vibration*, 458:109–122, 2019.

[44] J. Deng, O. Guasch, L. Maxit, and N. Gao. A metamaterial consisting of an acoustic black hole plate with local resonators for broadband vibration reduction. *Journal of Sound and Vibration*, 526:116803, 2022.

[45] W. Gao, Z. Qin, and F. Chu. Broadband vibration suppression of rainbow metamaterials with acoustic black hole. *International Journal of Mechanical Sciences*, 228:107485, 2022.

[46] X. Chen, J. Zhao, J. Deng, Y. Jing, H. Pu, and J. Luo. Low-frequency enhancement of acoustic black holes via negative stiffness supporting. *International Journal of Mechanical Sciences*, 241:107921, 2023.

[47] S. Quaegebeur, G. Raze, L. Cheng, and G. Kerschen. A virtual acoustic black hole on a cantilever beam. *Journal of Sound and Vibration*, 554:117697, 2023.

[48] V. Denis, A. Pelat, and F. Gautier. Scattering effects induced by imperfections on an acoustic black hole placed at a structural waveguide termination. *Journal of Sound and Vibration*, 362:56 – 71, 2016.

[49] S.C. Conlon, J.B. Fahnline, and F. Semperlotti. Numerical analysis of the vibroacoustic properties of plates with embedded grids of acoustic black holes. *The Journal of the Acoustical Society of America*, 137(1):447–457, 2015.

[50] S.C. Conlon and P.A. Feurtado. Progressive phase trends in plates with embedded acoustic black holes. *The Journal of the Acoustical Society of America*, 143(2):921–930, 2018.

[51] J. Leng, V. Romero-García, A. Pelat, R. Picó, J-P. Groby, and F. Gautier. Interpretation of the acoustic black hole effect based on the concept of critical coupling. *Journal of Sound and Vibration*, page 115199, 2020.

[52] V. Denis, A. Pelat, C. Touzé, and F. Gautier. Improvement of the acoustic black hole effect by using energy transfer due to geometric nonlinearity. *International Journal of Non-Linear Mechanics*, 94:134–145, 2017.

[53] H. Li, C. Touzé, A. Pelat, F. Gautier, and X. Kong. A vibro-impact acoustic black hole for passive damping of flexural beam vibrations. *Journal of Sound and Vibration*, 450:28–46, 2019.

[54] H. Li, C. Touzé, F. Gautier, and A. Pelat. Linear and nonlinear dynamics of a plate with acoustic black hole, geometric and contact nonlinearity for vibration mitigation. *Journal of Sound and Vibration*, 508:116206, 2021.

[55] H. Li, M. Sécail-Géraud, A. Pelat, F. Gautier, and C. Touzé. Experimental evidence of energy transfer and vibration mitigation in a vibro-impact acoustic black hole. *Applied Acoustics*, 182:108168, 2021.

[56] H. Li, C. Touzé, A. Pelat, and F. Gautier. Combining nonlinear vibration absorbers and the acoustic black hole for passive broadband flexural vibration mitigation. *International Journal of Non-Linear Mechanics*, page 103558, 2020.

[57] L. Zhang, G. Kerschen, and L. Cheng. Nonlinear features and energy transfer in an acoustic black hole beam through intentional electromechanical coupling. *Mechanical Systems and Signal Processing*, 177:109244, 2022.

[58] T. Zhou and L. Cheng. A resonant beam damper tailored with acoustic black hole features for broadband vibration reduction. *Journal of Sound and Vibration*, 430:174–184, 2018.

[59] M. Li, J. Deng, L. Zheng, and S. Xiang. Vibration mitigation via integrated acoustic black holes. *Applied Acoustics*, 198:109001, 2022.

[60] H. Ji, N. Wang, C. Zhang, X. Wang, L. Cheng, and J. Qiu. A vibration absorber based on two-dimensional acoustic black holes. *Journal of Sound and Vibration*, 500:116024, 2021.

[61] H. Ji, X. Zhao, N. Wang, W. Huang, J. Qiu, and L. Cheng. A circular eccentric vibration absorber with circumferentially graded acoustic black hole features. *Journal of Vibration and Acoustics*, 144(2), 2022. 021014.

[62] J. Deng, N. Gao, X. Chen, B. Han, and H. Ji. Evanescent waves in a metabeam attached with lossy acoustic black hole pillars. *Mechanical Systems and Signal Processing*, 191:110182, 2023.

[63] C. Issanchou, S. Bilbao, J.L. Le Carrou, C. Touzé, and O. Doaré. A modal-based approach to the nonlinear vibration of strings against a unilateral obstacle: Simulations and experiments in the pointwise case. *Journal of Sound and Vibration*, 393:229–251, 2017.

[64] T. Li, S. Seguy, and A. Berlioz. Optimization mechanism of targeted energy transfer with vibro-impact energy sink under periodic and transient excitation. *Nonlinear Dynamics*, 87:2415–2433, 2017.

[65] D. Qiu, S. Seguy, and M. Paredes. Design criteria for optimally tuned vibro-impact nonlinear energy sink. *Journal of Sound and Vibration*, 442:497–513, 2019.

[66] T. Theurich, A. F. Vakakis, and M. Krack. Predictive design of impact absorbers for mitigating resonances of flexible structures using a semi-analytical approach. *Journal of Sound and Vibration*, 516:116527, 2022.

[67] R. Chabrier, G. Chevallier, E. Foltête, and E. Sadoulet-Reboul. Experimental investigations of a vibro-impact absorber attached to a continuous structure. *Mechanical Systems and Signal Processing*, 180:109382, 2022.

[68] R. Chabrier, E. Sadoulet-Reboul, G. Chevallier, E. Foltête, and T. Jeannin. Full-field measurements with digital image correlation for vibro-impact characterisation. *Mechanical Systems and Signal Processing*, 156:107658, 2021.

[69] T. Theurich and M. Krack. Experimental validation of impact energy scattering as concept for mitigating resonant vibrations. *Journal of Structural Dynamics*, 2:1–23, 2023.

[70] C. Lalanne. *Mechanical Shock*. ISTE Ltd and John Wiley & Sons, Inc, London, Hoboken, 2009. Mechanical vibration and shock analysis, volume 2, second edition.

[71] F. Botta and G. Cerri. Shock response spectrum in plates under impulse loads. *Journal of Sound and Vibration*, 308(3-5):563–578, 2007.

[72] J. Wijker. *Mechanical Vibrations in Spacecraft Design*. Springer, Berlin, Heidelberg, 2004.